



Generating Shearing and Transverse Gusts through One-Dimensional Wind Tunnel Control

Brandon Lim*, Jennifer Lovell-Medina†, James L. Karr‡, and Xiaowei He§
University of Utah, Salt Lake City, Utah, 84112

A louver gust generator is placed downstream of the test section of a suction fan wind tunnel. Through individual controls of the louvers, the blockage effect is distributed in the transverse direction of the mean flow, creating a pressure gradient distribution. Hence, the streamwise velocity gradient in the transverse direction can be controlled by the gust generator. A potential flow method is used to pre-examine the test-section flow field under steady and unsteady blockage distributions. Wind tunnel control experiments are conducted, which include static and dynamic (oscillatory and traveling-wave) controls of the blockage distribution. The gust effect can propagate spatially under the traveling-wave blockage controls. Secondary velocity components are generated in dynamic control cases with the gust ratio varying from 0.06 to 0.85, depending on the frequency and wavelength. The experimental results show that the gust characteristics have dependency upon the wave frequency and wavelength, and agree with the potential flow predictions under certain dimensional wave speeds.

Nomenclature

B	= blockage created by the louver
c	= wave speed of traveling wave
\hat{c}	= normalized wave speed of traveling wave, $\hat{c} = c/u_0$
D	= transverse dimension (depth) of test section
f	= frequency, Hz
\hat{f}	= dimensionless frequency, $\hat{f} = f t_c$
f_{lpf}	= low-pass filter cut-off frequency, Hz
GR	= gust ratio
H	= vertical dimension (height) of test section
L	= streamwise dimension (length) of test section
T	= period
t	= time, second
t_c	= convective time, $t_c = D/u_0$
u	= streamwise velocity component
u_0	= mean flow speed
v	= spanwise/transverse velocity component
W	= complex velocity
x, y	= streamwise and spanwise coordinates
α_{flow}	= flow angle
θ	= louver angle, degree
λ	= wavelength of traveling wave
$\hat{\lambda}$	= normalized wavelength of traveling wave, $\hat{\lambda} = \lambda/D$
σ	= standard deviation
φ	= phase lag

*Graduate Research Assistant, Department of Mechanical Engineering, 1495 East 100 South, Salt Lake City, Utah 84112.

†Research Assistant, Department of Mechanical Engineering, 1495 East 100 South, Salt Lake City, Utah 84112.

‡Graduate Research Assistant, Department of Mechanical Engineering, 1495 East 100 South, Salt Lake City, Utah 84112.

§Assistant Professor, Department of Mechanical Engineering, 1495 East 100 South, Salt Lake City, Utah 84112; xiaowei.he@utah.edu. Member AIAA.

I. Introduction

PROGRESS in unsteady aerodynamics increasingly requires accurate analysis and in-depth understanding of the interactions between flying vehicles and the dynamic environments in which they are operated. Meanwhile, vehicle control applications involving advanced unsteady aerodynamic models and flow/flight control methods often need to be tested in certain unsteady flow conditions, including random gusts and sinusoidal waves. External gust disturbances introduce unsteady effects to aircraft, and the aerodynamic responses of the aircraft primarily depend on the airframe design and the gust profiles. The airframe is usually a fixed design of a particular aircraft. In contrast, the gust disturbances can vary regarding their amplitudes, spectra, length scales, and waveforms, therefore forming a complex parameter space of wing-gust interactions [1]. For studies on wing-gust interactions, a determined gust profile or spectrum is often preferred [2]. Therefore, controlled gust generation has its unique and essential role in unsteady aerodynamics.

Unsteady disturbances in wing-gust interaction studies can be realized through unsteady motions of the test objects, such as pitching [3, 4], plunging [5], rolling [6], surging [7], and combinations of multi-degree-of-freedom motions [8–13]. However, the types and profiles of the gusts that can be simulated by forced motions of the test objects are restricted by the fixed rotational centers and limited degrees of freedom of the physical mechanisms. For example, the unsteady features of a pitching-surging combined flow disturbance could not be replicated appropriately, although the pivot point was transferable relative to the model aircraft [13]. On the other hand, recent studies have focused on perturbations in the incoming flows, taking advantage of the versatile types of unsteady disturbances and closer characteristics regarding atmospheric gusts. Both stochastic and 1 – cosine types of flow disturbances are FAA certification requirements for assessing aircraft stability [14, 15]. Atmospheric turbulence was generated in wind tunnels with upstream active grids [16] and downstream [17] louver controls, where desired gust spectra, including von Kármán and Dryden gust spectra, were achieved at different Reynolds numbers. Concurrent progress in creating specific gust profiles was also achieved in wind and water tunnels through various perturbation methods. Louver mechanisms are utilized in wind tunnels to generate large-scale turbulence [17], surging flows [18], periodic oscillating flows [19], and traveling waves [20]. Active grids [21–24] and distributed fans [25, 26] are also efficient methods to create turbulence at various length scales or specific velocity profiles in certain directions. For two-dimensional or traveling-wave gusts, direct jet and towing [27, 28], jet-vortex-generator arrays [29], wall perturbations [30], single and sequent vortices generators [31, 32], and suction-driven methods [20] are some of the recent developments of providing such flow environments for wing-gust interactions and unsteady aerodynamics experiments.

One complicated aspect of gust encounters that draws substantial research efforts and continues to require further investigation is the transient process and the aerodynamic response thereof. Transient processes in wing-gust interactions are introduced by the temporal and spatial characteristics of the gusts acting on the test objects [2]. The temporal unsteadiness can be described by the effective accelerations experienced by the test objects in forced motions, such as pitching [3, 4], or homogeneous flow perturbations, typically surging [33–35]. The spatial characteristics of the gusts are of increasing interest due to their sophisticated local aerodynamic effects and similarity to atmospheric flow disturbances in real flight conditions. Spatial variations of the gust profile are concerned with the creation of velocity gradients [20, 26, 36] or propagation of specific flow structures, such as vortices [31]. A high gust ratio is often preferred to expose the transient process in wing-gust interactions. However, it is also challenging to achieve in experiments despite some recent progress [37]. On the other hand, the ability to generate designated velocity gradients in different directions is essential for replicating gust profiles from classical unsteady aerodynamic theories, such as Küssner [38], Wagner [39, 40], Sears [41], and Atassi [42]. It is also critical to the propagation of traveling waves that the velocity gradients are controlled accordingly to the waveforms. For two-dimensional gusts, the velocity gradient tensor consists of two diagonal elements, $\partial u / \partial x$ and $\partial v / \partial y$, and two off-diagonal elements, $\partial u / \partial y$ and $\partial v / \partial x$. The off-diagonal velocity gradients have been achieved through transverse jets combined with streamwise motion [28] and propagated transverse suction [20] for $\partial v / \partial x$; meanwhile, $\partial u / \partial y$ disturbances have been generated by upstream grids or flaps [19, 36], through which $\partial u / \partial y$ is coupled with $\partial v / \partial x$. For the diagonal velocity gradients, however, large-scale perturbations are hard to generate in experiments, especially regarding the accurate control of the streamwise gradient, $\partial u / \partial x$ [17, 35].

This work uses a downstream louver mechanism to control the temporal and spatial variation of the velocity in the transverse direction, aiming to generate a traveling-type gust profile. The challenge is that the gust generator and its control are one-dimensional and are perpendicular to the gust propagating direction. However, though distributed blockage effects in the transverse direction, $\partial p / \partial x$ can be controlled as a function of y , thus providing an opportunity to control transverse gusts with a simple louver setup. The gust generator setup is introduced in [section II](#). Using a potential flow modeling approach [20], the traveling-wave gust profiles and associated gust ratios can be preliminarily estimated, which is described in [section III](#). The real-time experiments in [section IV](#) will show the gust generation

capability and the flow characteristics of the gusts.

II. Experimental Setup

A. Wind Tunnel Setup

The gust generation experiments and measurements are conducted in the low-speed wind tunnel at the University of Utah. The wind tunnel is a suction-fan, open-circuit wind tunnel with a maximum flow speed of 40 m/s. The test section was designed for boundary layer flow experiments, of which the total length is 6 m, and the cross-section area is variable. However, only the beginning section ($0 \leq L \leq 2.5$ m), where the cross-section dimensions are fixed at $H \times D = 0.62 \text{ m} \times 0.92 \text{ m}$, is used for the gust generation experiments in this paper. The gust profile is controlled by a gust generator that was placed at $L = 2.5$ m. The gust generator consisted of six louver mechanisms that are vertically installed on a frame and occupied the entire test section. Each louver is driven by a Teknic ClearPath CPM-MCPV-2311S-RLN servo motor independently to control the corresponding louver angle, θ_i , so the blockage, B_i , is independently controlled to vary from 0 (fully open) to 1 (fully blocked) with a conversion of $B_i = \sin \theta_i$ ($0^\circ \leq \theta_i \leq 90^\circ$).

When all louvers are uniformly controlled, the wind tunnel generates surging flows similarly to Refs. [17, 33]. When there is a blockage differential among the louvers, as illustrated in the schematic top view of the test section in fig. 1, a velocity gradient of the streamwise velocity in the transverse direction $\partial u / \partial y$ is expected to appear in the upstream flow. Besides the gradient of the u -velocity component, which creates the shearing flow characteristics, the pressure differential due to the flow speed difference in the transverse direction will also deflect the flow in the y direction, therefore creating a secondary v -velocity component.

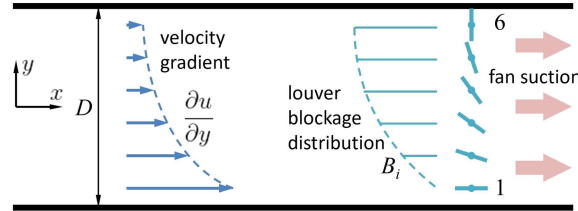


Fig. 1 Schematic top view of the gust generator in the test section and the coordinates.

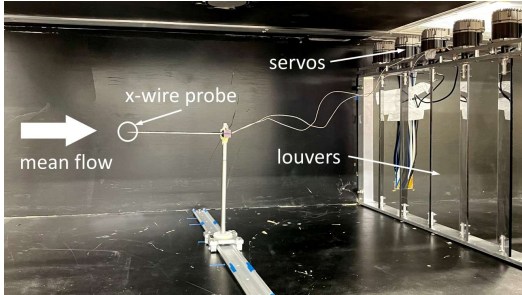
The servo controls and data acquisition of the flow measurements are built upon a dSPACE MicroLabBox I system operating at a sampling rate of 1 000 samples/s. A Dantec 55P61 x-wire probe using the Dantec MiniCTA anemometers is used to obtain the two-dimensional velocity components. The x wire is calibrated with a Dantec StreamLine Pro calibrator from 0.5 m/s to 17 m/s. The uncertainty in total velocity measurement is ± 0.22 m/s. Within $\pm 20^\circ$ flow angle, the maximum error levels for u component and v component are 0.57% and 2.7%, respectively. The x-wire signals are filtered by a low-pass filter at a cut-off frequency of $f_{lpf} = 30$ Hz. The u and v velocities are measured at five probe locations (y_1 to y_5) across the $0.8D$ test-section span with a uniform $0.2D$ spacing, as shown in fig. 2. The probe locations are one D distance upstream of the louvers. A positive flow angle is defined in the counterclockwise direction, aligned with the coordinate definition.

B. Test Cases

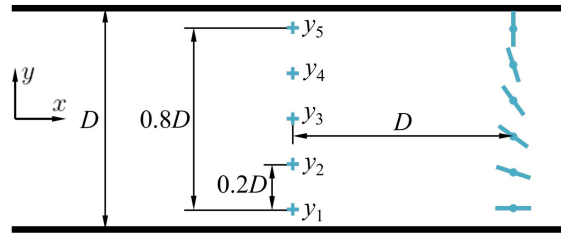
The wind tunnel response to the blockage control is characterized by static blockage cases and dynamic blockage cases. All test cases are conducted at freestream speeds of 5 m/s and 10 m/s, respectively, which correspond to unit-length Reynolds numbers $Re/L = 3.236 \times 10^5 \text{ m}^{-1}$ and $Re/L = 6.472 \times 10^5 \text{ m}^{-1}$.

The static cases use fixed, uniform blockage for all louvers, so $B_i = \bar{B} \in [0, 0.2, 0.4, 0.6, 0.8, 1]$. The velocity measurements at the five probe locations can provide a mapping between the blockage effect and the streamwise velocity.

The dynamic cases consist of oscillatory blockage controls and traveling-wave blockage controls. For oscillatory controls, the mean blockage \bar{B} varies sinusoidally from 0 to 1 at a few frequencies. There are semi-uniform cases where the blockages of half of the louvers are zeros, while the blockages of the other half vary at the same set of frequencies. The uniform and semi-uniform oscillatory blockage inputs are shown in table 1. For the frequencies used in the dynamic cases, the corresponding non-dimensional frequencies are obtained by $\hat{f} = f t_c = f D / u_0$.



(a) X-wire instrumented in the test section



(b) Probe positions

Fig. 2 Flow velocity measurement setup.

Table 1 Test cases for oscillatory blockage controls.

type	f [Hz]			
$B_i = \bar{B} = \frac{1}{2} \sin 2\pi f t + \frac{1}{2}$	0.5	1.0	1.5	2.0
$B_{1-3} = 0, B_{4-6} = \frac{1}{2} \sin 2\pi f t + \frac{1}{2}$	0.5	1.0	1.5	2.0

In the traveling-wave control cases, the blockage inputs are determined by a one-sided $1 - \cos$ wave function [20, 43, 44]

$$B(y, t) = \frac{1}{2} \left[1 - \cos \left(\frac{2\pi f}{c} y - 2\pi f t \right) \right], \quad (1)$$

where f is the wave frequency and c is the wave speed. The blockage of individual louvers B_i can be obtained by plugging in the corresponding coordinates y_i .

The frequencies are the same as the oscillatory control cases, and the wave speeds are at 0.6 m/s and 1.2 m/s, which determine the wavelength $\lambda = c/f$, as shown in table 2. With two mean flow speeds, a total number of 16 test cases are listed table 3, where all parameters are normalized. Note that the wavelengths are independent of the mean flow speeds.

Table 2 Test cases and corresponding wavelengths, λ [m], for traveling-wave blockage controls.

	f [Hz]			
	0.5	1	1.5	2
$c = 0.6$ m/s	1.2	0.6	0.4	0.3
$c = 1.2$ m/s	2.4	1.2	0.8	0.6

III. Potential Flow Simulation

A. Simulation Setup

Based on the panel method, a two-dimensional potential flow model is used to simulate the wind tunnel velocity field. Since potential flows solely depend on the boundary conditions, the dynamics of the flow field responding to the time-varying controls are not captured by the potential flow simulations. Nevertheless, we only use the simulation as a first estimation of the flow field to guide the experiments. Each louver and both walls are assumed to be zero-thickness plates with 99 panels on each plate.

The potential flow solutions for different louver blockage configurations can be solved with the geometries accordingly. When a time-varying blockage function is discretized in time, time-series snapshots of the potential flow field can be

Table 3 Normalized test case parameters and corresponding wavelengths, $\hat{\lambda}$, for traveling-wave blockage controls under $u_0 = 10$ m/s (values in parentheses are under $u_0 = 5$ m/s).

	\hat{f}			
	0.046 (0.092)	0.092 (0.138)	0.138 (0.184)	0.184 (0.368)
$\hat{c} = 0.06 (0.12)$	1.30	0.65	0.43	0.33
$\hat{c} = 0.12 (0.24)$	2.61	1.30	0.87	0.65

obtained to pre-examine the influence of the changing blockage distribution (without dynamics such as the transient process).

B. Estimations of velocity components

By implementing eq. (1) in the potential flow simulation. The quasi-steady flow fields under traveling-wave blockage controls can be solved, where the velocity components and the flow angle can be extracted at the $(-D, 0)$ point. In fig. 3, from left to right are two snapshots of the blockage distributions (individual inputs B_i as yellow square data points and continuous wave form $B(y)$ as dotted curves) and the corresponding flow fields as in gray streamlines. The flow field varies in space and time as the blockage peak propagates from louver 1 ($y = -0.4D$) to louver 6 ($y = 0.4D$). The blue arrow indicates the instantaneous velocity vector at the $(-D, 0)$ point, which also shows the flow angle oscillation within one wave period/wavelength. Intuitively, the velocity vector always points toward the least-blocked portion of the louvers, since the momentum concentrates toward the low-fluid-resistance area.

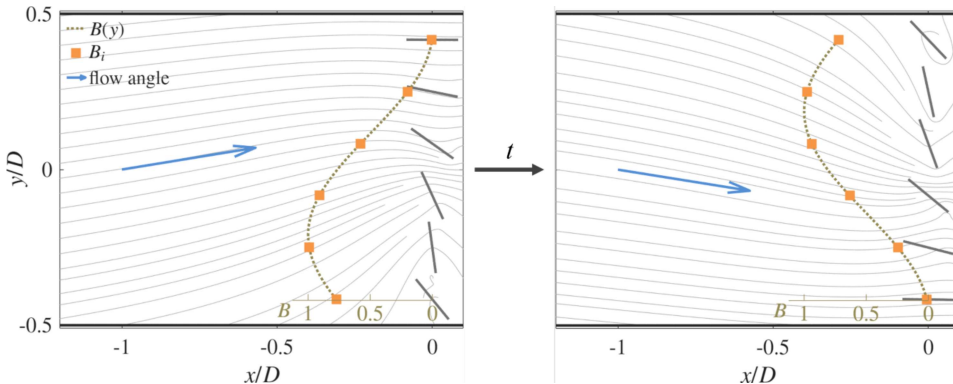


Fig. 3 Simulation flow fields under traveling-wave blockage control.

The time-series data across the wave frequencies and wavelengths can be extracted at the $(-D, 0)$ point, as shown in fig. 4. The u -, v -velocity components and the flow angle at $u_0 = 10$ m/s are grouped by the wavelengths as examples of the time-series data. The mean values of u components are lowered since the net blockage is always nonzero at any instant. The oscillation of the u components is due to the change in the total blockage and the local oscillation of the blockage effect. The phase of the u components also has a dependency on the phase of the blockage wave. In contrast, the v components of all cases are symmetric about the half-period point. The phase is locked to the phase of the blockage wave. When the peak of the blockage wave is at the negative half of the y coordinate, the flow is deflected to the positive direction in the flow field, which is shown as the positive values in the first-half period ($0 - 0.5T$). The second-half period shows the opposite v profiles as the blockage peak continues to propagate to the positive y coordinates. When the blockage trough and peak pass $y = 0$, where the time-series data are extracted, the flow field is symmetric about $y = 0$, which results in $v = 0$. The flow angle aligns with the variation of v in all cases, despite the variations in u velocities.

The gust ratio $GR = v_{\max}/\bar{u}$ [2] is evaluated for all 16 cases of combinations of frequency and wavelengths, as shown in fig. 5. The data points are grouped by their dimensional wavelengths and plotted against their normalized frequencies. The gust ratio does not show a monotonic dependency on the wave frequency. However, the groups with the same dimensional wave speed show the same trend of change in the gust ratio, which are not affected by the mean flow speed, i.e., the normalized wave speed. In addition, the normalized wavelengths calculated for each data point show that, in simulation, the gust ratio is correlated with the normalized wavelength; that is, the gust ratio will be the same if

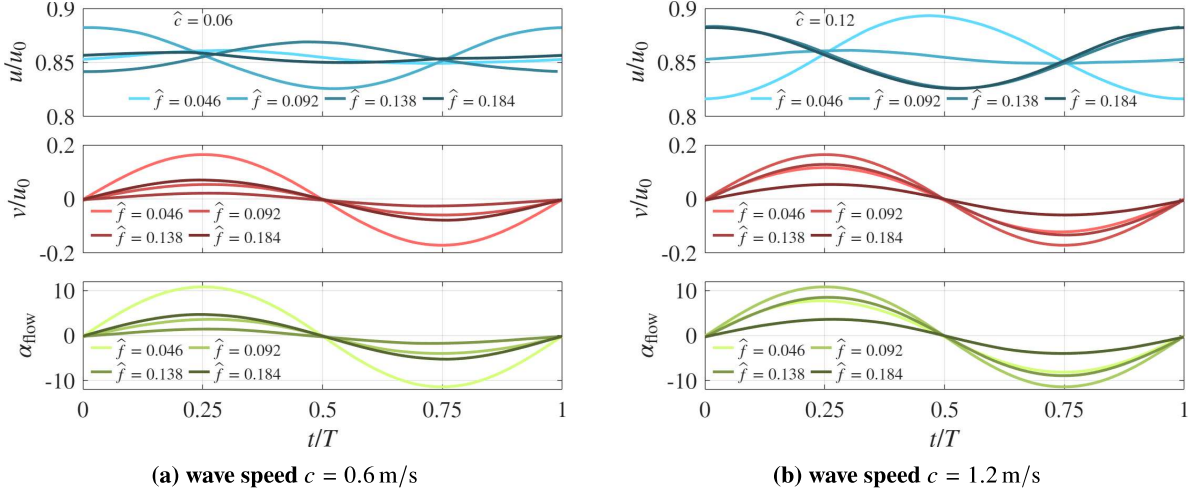


Fig. 4 Temporal velocity and flow angle variations at $(-D, 0)$ point at $u_0 = 10 \text{ m/s}$ in simulation.

two or more cases have the same normalized wavelength.

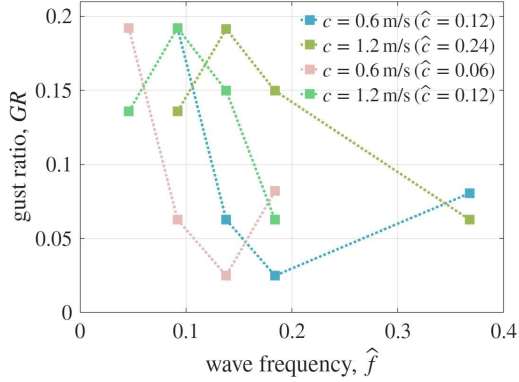


Fig. 5 Gust ratios of simulated cases.

IV. Experimental Results and Discussion

A. Static Baselines

Static baselines are obtained by using the uniform blockage input described in section II.B. The flow speed measurements at the five probe locations under the two mean flow speeds are shown in fig. 6. Each vertical line of data points is a spatial distribution under a uniform blockage input. The error bars represent the 2σ uncertainty. The measurements show that the flow is sufficiently uniform across the span. The normalized flow speed slows down from 1 to 0.31 as the blockage increases from 0 to 1. The flow speed for $\bar{B} = 1$ is nonzero due to the leakage of the louver mechanism; in particular, the servo portion is not sealed.

The spatial average flow speeds over five measurements under each blockage setting compose the $u-\bar{B}$ curves in fig. 7a. The two curves at $u_0 = 5 \text{ m/s}$ and $u_0 = 10 \text{ m/s}$ overlap. The $u-\bar{B}$ relation is nonlinear. However, a linear relation is found between u^2 and \bar{B}^2 , where $\hat{u}^2 = -0.89\bar{B}^2 + 0.99$ for both mean flow speeds, as shown in fig. 7b.

B. Dynamic Oscillations

The dynamic oscillation tests use sinusoidal blockage inputs at frequencies given in section II.B, which corresponds to two groups of normalized frequencies depending on the mean flow speeds. The results of the uniform oscillation

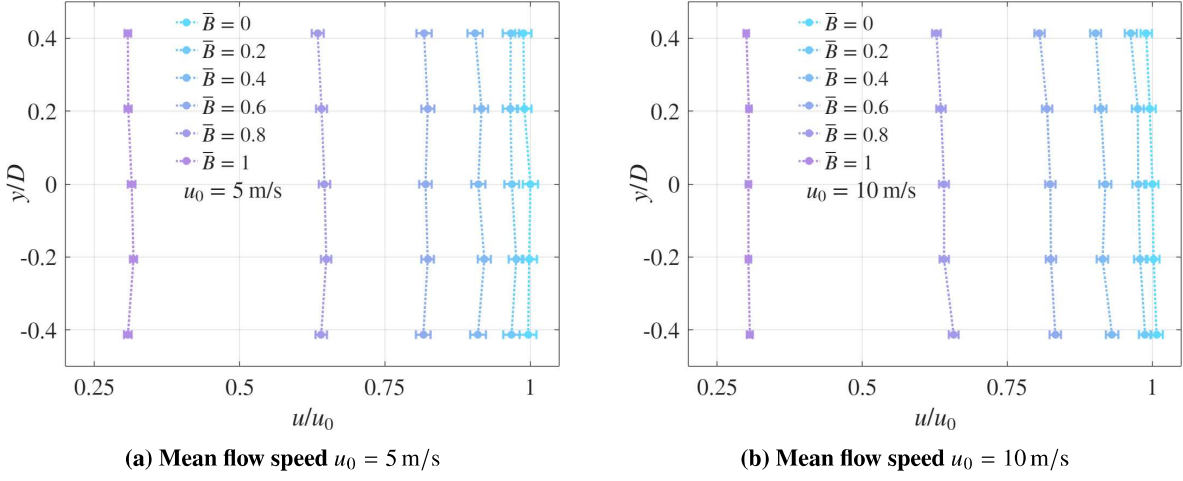


Fig. 6 Spatial distribution of flow speeds under static, uniform blockage settings.

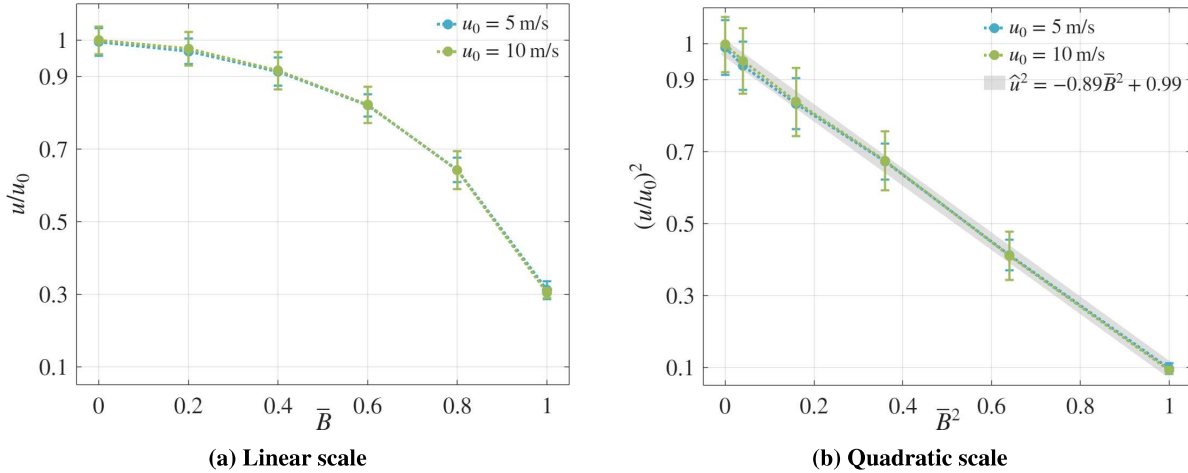


Fig. 7 Spatially averaged flow speed vs. static, uniform blockage settings.

cases at the two mean flow speeds are shown in figs. 8a and 8b, respectively. The data are the u -velocity measurements at the $(-D, 0)$ point and are cycle-averaged over 60 to 240 cycles, increasing with the frequency. The shaded areas indicate the 2σ standard deviations. The black curve indicates the one-sided sine wave blockage during one normalized period. The blue curves are the u -velocity responses. The responses are not entirely sinusoidal because there exists an asymmetric motion in the louver rotation, where the reversal is sharper as $\bar{B} \rightarrow 1$ than as $\bar{B} \rightarrow 0$. Nevertheless, the u velocities are symmetric about their means, and their amplitudes scale with the normalized frequencies, where the cases with the same \hat{f} have similar amplitudes, such as at $\hat{f} = 0.092$ and $\hat{f} = 0.184$.

Phase differences are observed between the u velocities and the blockage inputs. Figure 9 shows that the velocity responses are lagging (with positive phase lags) the blockage inputs. Overall, the phase difference between the output and input increases as the oscillation frequency increases.

The semi-uniform dynamic oscillation tests are carried out by maintaining half of the louvers (louvers 1 to 3) fully open, while the oscillations are implemented only to the other half (louvers 4 to 6). The flow measurements are recorded at the $(-D, 0)$ and $(-D, -0.2D)$ points, of which the results are shown in fig. 10. The drop in the average u velocity is not as significant as that of the uniform oscillation cases. However, the characteristics of the amplitude scaling and phase shift with respect to the frequency remain the same trends. Since the flow fields are asymmetric in these cases, the flow angles (green curves) are also included in the plots to demonstrate the influence of the secondary velocity component. The flow angles are all negative because the flow is always deflected to the negative y direction, as louvers 1 to 3 are always fully open. The flow angles measured at $(-D, 0)$ (figs. 10a and 10b) have larger amplitudes than at

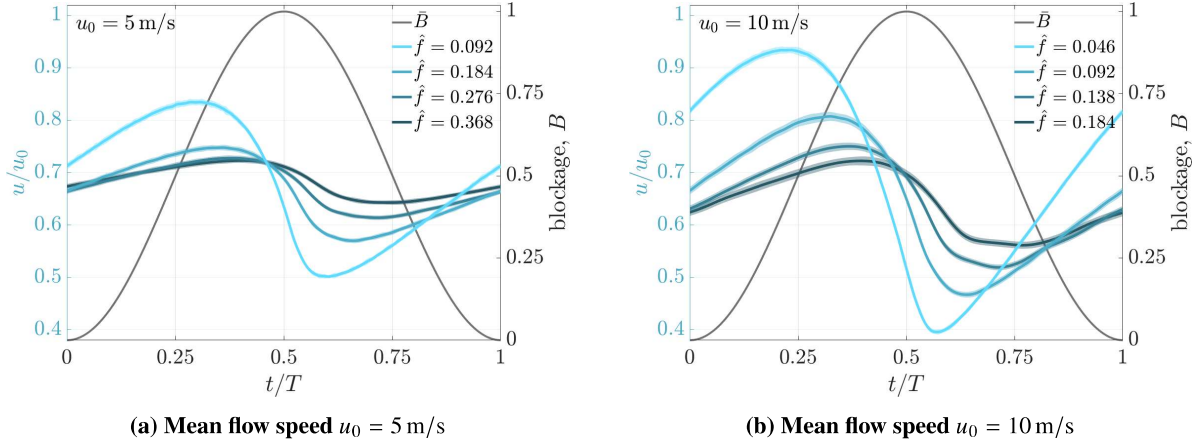


Fig. 8 Temporal measurements of flow speed at $(-D, 0)$ point under uniform, sinusoidal blockage controls.

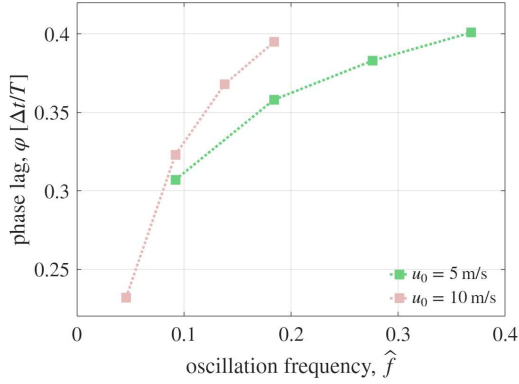


Fig. 9 Phase lag between the u velocity and the blockage input.

$(-D, -0.2)$ (figs. 10c and 10d). This is due to the flow being “flatter” closer to the wind tunnel wall, which also showed up in the potential-flow simulated flow fields. In general, the flow angle amplitude decreases with increasing frequency, and its phase lag increases with the frequency, which is consistent with the uniform oscillation cases.

C. Traveling-wave controls

Traveling-wave blockage control inputs are employed with the intention of generating spatially propagating gusts in the transverse direction. According to table 1, sixteen traveling-wave cases are examined with flow measurements recorded at all five probe locations. The measurements are cycle-averaged over 60 to 240 cycles, depending on the frequency, similar to the dynamic oscillation cases. As example cases, the results of cases at $f = 0.5 \text{ Hz}$ are shown in fig. 11. The plots demonstrate the snapshots of spatial variations of the velocity components and the flow angle at four phases between $\frac{1}{8}T$ and $\frac{1}{2}T$. From left to right are the u velocity, v velocity, flow angle α_{flow} , and the blockage input. The solid data points are the experimental measurements or inputs. The dotted curves are fourth-order polynomial fits of the data points or the calculated sinusoidal curves to help observation. The arrows with gradient colors indicate the direction of wave propagation, which is also the direction of time. Darker colored data points and curves represent later phases in the cycle.

Similar to the oscillation cases, the average u velocity is lowered due to the nonzero blockage at any instant. In most cases, this drop is within $0.3u_0$. The exception in fig. 11d, where the average drops by $0.6u_0$. As the peaks or troughs of the blockage waves travel from negative to positive y coordinates, there exist apparent wave propagating features in both velocity components, as well as the flow angle. The traveling pattern is mainly observable in the v velocity, which results in the propagation of the flow angle across the span. We noted that the amplitude of the v velocity variation is an order of magnitude lower than that of the simulation results. However, the sign of the gust/flow angle follows the exact mechanism found in the simulation results if examined with the blockage propagation. The direction of the gust points

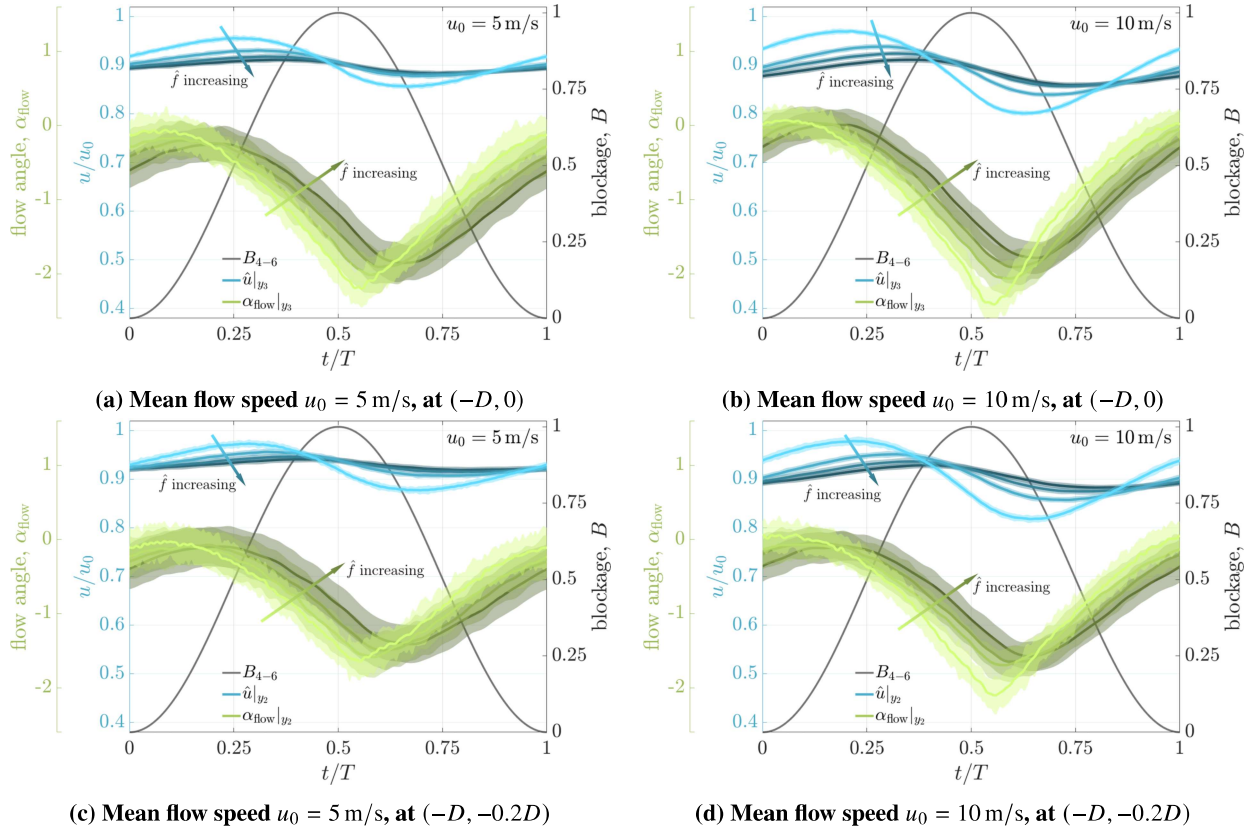


Fig. 10 Temporal measurements of flow speed under semi-uniform, sinusoidal controls.

toward the low blockage portion on the span, and the flow field tends to be more symmetric about the location where the highest blockage appears. This pattern is observed in all tested cases, especially those with shorter wavelengths.

Similar to fig. 4, the time-series data can be plotted for fixed-point measurements. Figure 12 combined show the time-series data at $(-D, 0)$ for all 16 tested case. For the experimental results, there is no common symmetric point in the v -velocity data, which indicates that the phases of the velocity responses are shifted as the frequency changes. This dynamic effect can not be captured by the steady-state simulations. The amplitude of velocity oscillation is nonmonotonic with respect to the frequency increment, which agrees with the simulation results.

The velocity fluctuations can be quantified by the gust ratios shown in fig. 13. The data points are still grouped by their dimensional wave speeds at the two mean flow speeds and plotted with respect to the frequency. Although the absolute values are shifted, the groups that have the same dimensional wave speed carry the same pattern of change, and the patterns agree with those in the simulation results. The correlation to the normalized wavelength still exists, especially at lower normalized frequencies.

V. Conclusion

A method for generating transverse gusts using a one-dimensional louver-based control system was applied to a wind tunnel. By independently controlling the louvers, spatial variations in blockage were introduced across the span, enabling control over transverse pressure gradients and inducing velocity gradients upstream of the louvers. The system produced measurable variations in both the streamwise and transverse velocity components. This confirmed that lateral velocity gradients and secondary flow can be induced without requiring two-dimensional or upstream actuation.

Experimental tests under static, oscillatory, and traveling-wave control conditions were conducted to evaluate the gust generator's performance. Static tests demonstrated the quadratic relationship between blockage and mean streamwise velocity. Oscillatory controls showed predictable amplitude scaling and increasing phase lag with frequency, though some asymmetries were observed due to the mechanical characteristics of the louver system. In traveling-wave cases, transverse velocity variations and wave-like flow angle patterns were detected, indicating the generation of spatially

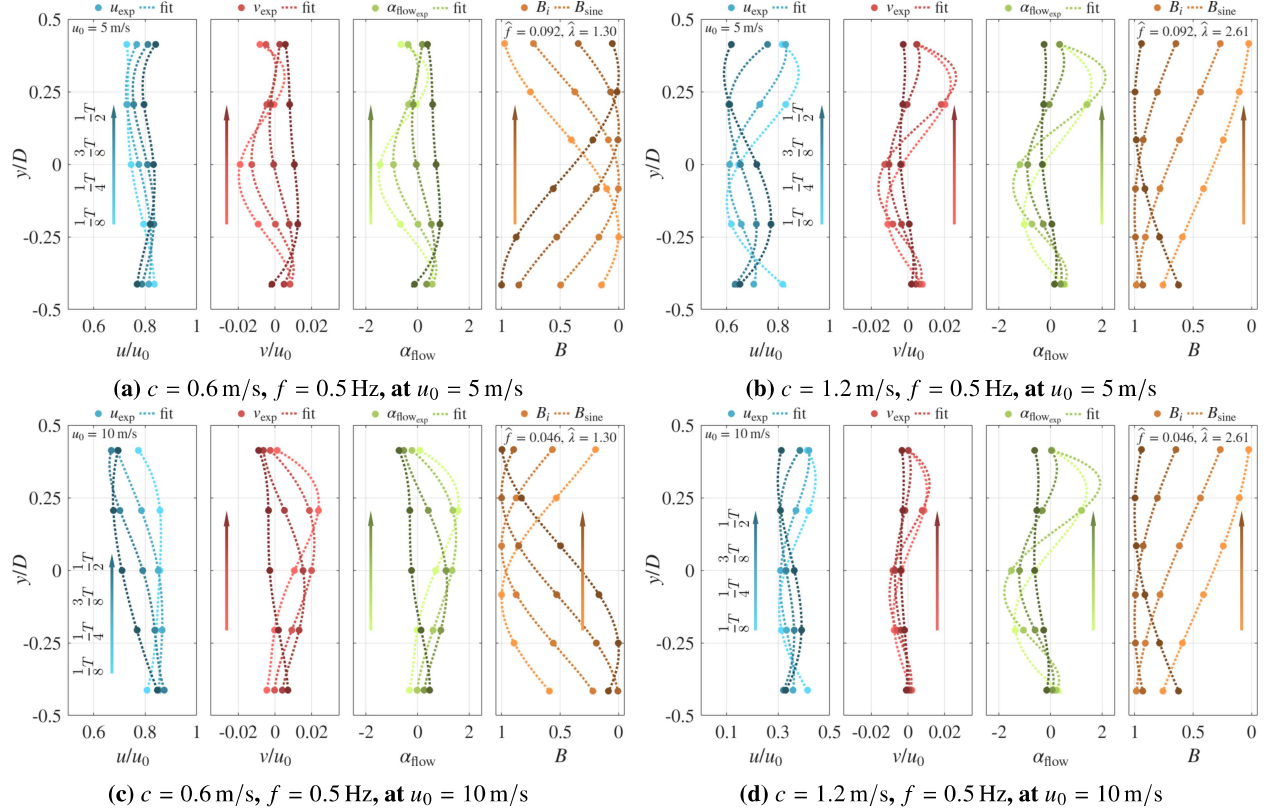


Fig. 11 Spatial variation of flow characteristics under traveling-wave blockage controls.

propagating gusts. However, the amplitude of transverse velocity components was lower than predicted, and gust ratios remained modest (on the order of 0.06–0.85) across the tested conditions.

Overall, the results show that the louver system provides a practical method to induce controlled transverse flow variations, with observable wave-like features under certain conditions. While the gust strength was limited, the setup offers a straightforward approach to studying simplified gust interactions and may be useful for exploring unsteady aerodynamic responses in controlled laboratory settings.

References

- [1] Jones, A. R., “Gust encounters of rigid wings: Taming the parameter space,” *Physical Review Fluids*, Vol. 5, 2020, p. 110513. <https://doi.org/10.1103/PhysRevFluids.5.110513>.
- [2] Jones, A. R., and Cetiner, O., “Overview of Unsteady Aerodynamic Response of Rigid Wings in Gust Encounters,” *AIAA Journal*, Vol. 59, No. 2, 2021, pp. 731–736. <https://doi.org/10.2514/1.J059602>.
- [3] An, X., Williams, D. R., Eldredge, J. D., and Colonius, T., “Lift Coefficient Estimation for a Rapidly Pitching Airfoil,” *Experiments in Fluids*, Vol. 62, No. 1, 2021, 11. <https://doi.org/10.1007/s00348-020-03105-3>.
- [4] Deparday, J., and Mullenens, K., “Modeling the Interplay between the Shear Layer and Leading Edge Suction during Dynamic Stall,” *Physics of Fluids*, Vol. 31, No. 10, 2019, p. 107104. <https://doi.org/10.1063/1.5121312>.
- [5] Perrotta, G., and Jones, A. R., “Quasi-Steady Approximation of Forces on Flat Plate due to Large-Amplitude Plunging Maneuvers,” *AIAA Journal*, Vol. 56, No. 11, 2018, pp. 4232–4242. <https://doi.org/10.2514/1.J057194>.
- [6] He, X., Le Provost, M., and Williams, D. R., “Dynamic Active Flow Control of the Roll Moment on a Generic UCAS Wing,” *2018 AIAA Aerospace Sciences Meeting*, 2018. <https://doi.org/10.2514/6.2018-0327>, AIAA Paper 2018-0327.
- [7] Granlund, K., Monnier, B., Ol, M., and Williams, D., “Airfoil longitudinal gust response in separated vs. attached flows,” *Physics of Fluids*, Vol. 26, No. 2, 2014, p. 027103. <https://doi.org/10.1063/1.4864338>.

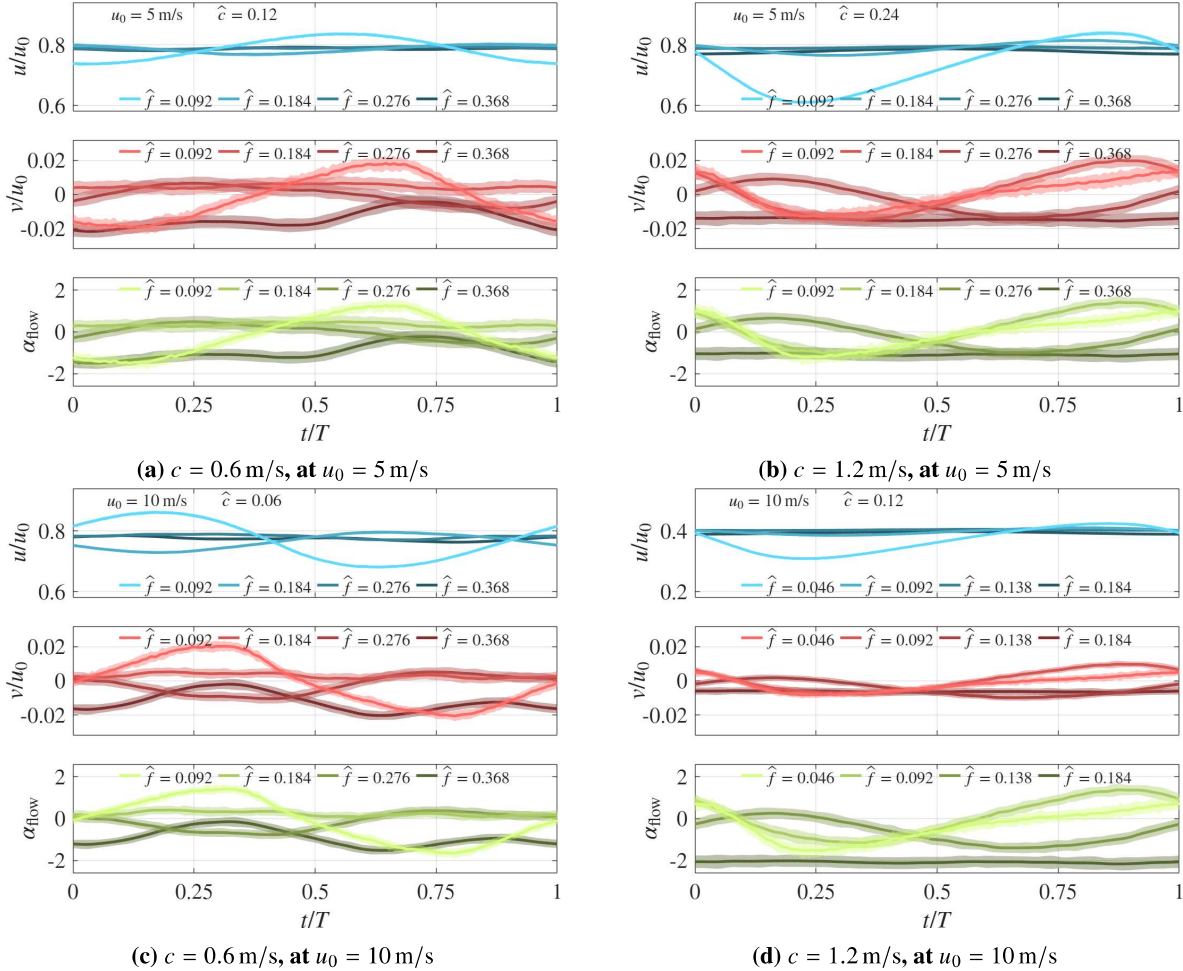


Fig. 12 Temporal measurements of velocity and flow angle at the $(-D, 0)$ point.

- [8] Favier, D., Agnes, A., Barbi, C., and Maresca, C., “Combined translation/pitch motion - A new airfoil dynamic stall simulation,” *Journal of Aircraft*, Vol. 25, No. 9, 1988, pp. 805–814. <https://doi.org/10.2514/3.45663>.
- [9] Laitone, E. V., “Dynamic stall on a pitching and surging airfoil,” *Experiments in Fluids*, Vol. 23, No. 5, 1997, pp. 405–409. <https://doi.org/10.1007/s003480050128>.
- [10] Dunne, R., and McKeon, B. J., “Dynamic stall on a pitching and surging airfoil,” *Experiments in Fluids*, Vol. 56, No. 8, 157, 2015. <https://doi.org/10.1007/s00348-015-2028-1>.
- [11] Leung, J. M., Wong, J. G., Weymouth, G. D., and Rival, D. E., “Modeling Transverse Gusts Using Pitching, Plunging, and Surging Airfoil Motions,” *AIAA Journal*, Vol. 56, No. 8, 2018, pp. 3271–3278. <https://doi.org/10.2514/1.J059658>.
- [12] Medina, A., Ol, M. V., Greenblatt, D., Müller-Vahl, H., and Strangfeld, C., “High-Amplitude Surge of a Pitching Airfoil: Complementary Wind- and Water-Tunnel Measurements,” *AIAA Journal*, Vol. 56, No. 4, 2018, pp. 1703–1709. <https://doi.org/10.2514/1.J056408>.
- [13] He, X., and Williams, D. R., “Unsteady Aerodynamic Loads on a UAS Model during a Pitch Maneuver with Roll,” *AIAA Scitech 2020 Forum*, 2020. <https://doi.org/10.2514/6.2020-0822>, AIAA Paper 2020-0822.
- [14] Hoblit, F. M., *Gust Loads on Aircraft: Concepts and Applications*, American Institute of Aeronautics and Astronautics, New York, NY, 1988.
- [15] FAA, “Dynamic Gust Loads,” Tech. rep., Federal Aviation Administration, 2014. AC 25.341-1.

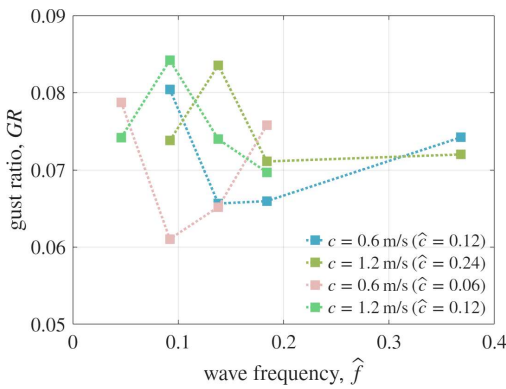


Fig. 13 Gust ratios of traveling-wave controlled cases.

- [16] Neuhaus, L., Hölling, M., Bos, W. J. T., and Peinke, J., “Generation of Atmospheric Turbulence with Unprecedentedly Large Reynolds Number in a Wind Tunnel,” *Physical Review Letters*, Vol. 125, 2020, p. 154503. <https://doi.org/10.1103/PhysRevLett.125.154503>.
- [17] He, X., and Williams, D. R., “Spectral Feedback Control of Turbulent Spectra in a Wind Tunnel,” *Experiments in Fluids*, Vol. 61, No. 8, 2020, p. 175. <https://doi.org/10.1007/s00348-020-03003-8>.
- [18] Farnsworth, J., Sinner, D., Gloutak, D., Droste, L., and Bateman, D., “Design and qualification of an unsteady low-speed wind tunnel with an upstream louver system,” *Experiments in Fluids*, Vol. 61, No. 8, 2020, p. 181. <https://doi.org/10.1007/s00348-020-03018-1>.
- [19] Wei, N. J., Kissing, J., Wester, T. T. B., Wegt, S., Schiffmann, K., Jakirlic, S., Hölling, M., Peinke, J., and Tropea, C., “Insights into the Periodic Gust Response of Airfoils,” *Journal of Fluid Mechanics*, Vol. 876, 2019, pp. 237–263. <https://doi.org/10.1017/jfm.2019.537>.
- [20] He, X., Williams, D. R., and Dawson, S. T. M., “Transverse gust generation in a wind tunnel: a suction-driven approach,” *Experiments in Fluids*, Vol. 63, No. 8, 2022, p. 125. <https://doi.org/10.1007/s00348-022-03484-9>.
- [21] Makita, H., “Realization of a Large-Scale Turbulence Field in a Small Wind Tunnel,” *Fluid Dynamics Research*, Vol. 8, No. 1–4, 1991, pp. 53–64. [https://doi.org/10.1016/0169-5983\(91\)90030-M](https://doi.org/10.1016/0169-5983(91)90030-M).
- [22] Roadman, J. M., and Mohseni, K., “Large Scale Gust Generation for Small Scale Wind Tunnel Testing of Atmospheric Turbulence,” *39th AIAA Fluid Dynamics Conference*, 2009. <https://doi.org/10.2514/6.2009-4166>, AIAA Paper 2009-4166.
- [23] Knebel, P., Kittel, A., and Peinke, J., “Atmospheric Wind Field Conditions Generated by Active Grids,” *Experiments in Fluids*, Vol. 51, No. 2, 2011, pp. 471–481. <https://doi.org/10.1007/s00348-011-1056-8>.
- [24] Larssen, J. V., and Devenport, W. J., “On the generation of large-scale homogeneous turbulence,” *Experiments in Fluids*, Vol. 50, No. 5, 2011, pp. 1207–1223. <https://doi.org/10.1007/s00348-010-0974-1>.
- [25] Lawson, J. M., and Ganapathisubramani, B., “Unsteady forcing of turbulence by a randomly actuated impeller array,” *Experiments in Fluids*, Vol. 63, No. 1, 2021, p. 13. <https://doi.org/10.1007/s00348-021-03364-8>.
- [26] Li, S., Liu, Y., Jiang, Z., Hu, G., Noack, B. R., and Raps, F., “Aerodynamic Characterization of a Fan-Array Wind Generator,” *AIAA Journal*, Vol. 62, No. 1, 2024, pp. 291–301. <https://doi.org/10.2514/1.J063114>.
- [27] Corkery, S. J., Babinsky, H., and Harvey, J. K., “On the Development and Early Observations from a Towing Tank-Based Transverse Wing–Gust Encounter Test Rig,” *Experiments in Fluids*, Vol. 59, No. 9, 135, 2018. <https://doi.org/10.1007/s00348-018-2586-0>.
- [28] Biler, H., Badrya, C., and Jones, A. R., “Experimental and Computational Investigation of Transverse Gust Encounters,” *AIAA Journal*, Vol. 57, No. 11, 2019, pp. 4608–4622. <https://doi.org/10.2514/1.J057646>.
- [29] Olson, D. A., Naguib, A. M., and Koochesfahani, M. M., “Development of a Low-Turbulence Transverse-Gust Generator in a Wind Tunnel,” *AIAA Journal*, Vol. 59, No. 5, 2021, pp. 1575–1584. <https://doi.org/10.2514/1.J059962>.

- [30] Fernandez, F., Cleaver, D., and Gursul, I., "Unsteady Aerodynamics of a Wing in a Novel Small-Amplitude Transverse Gust Generator," *Experiments in Fluids*, Vol. 62, No. 1, 9, 2021. <https://doi.org/10.1007/s00348-020-03100-8>.
- [31] Qian, Y., Wang, Z., and Gursul, I., "Interaction of quasi-two-dimensional vortical gusts with airfoils, unswept and swept wings," *Experiments in Fluids*, Vol. 63, No. 8, 2022, p. 124. <https://doi.org/10.1007/s00348-022-03477-8>.
- [32] Bricker, C., Bull, S., Gursul, I., and Young, A. M., "Characterization of Novel Large Amplitude Gust Generator," *AIAA SCITECH 2025 Forum*, 2025. <https://doi.org/10.2514/6.2025-2765>, AIAA Paper 2022-0044.
- [33] He, X., and Williams, D. R., "Unsteady Aerodynamic Loads on an Airfoil at High Angle of Attack in a Randomly Surging Flow," *AIAA Scitech 2020 Forum*, 2020. <https://doi.org/10.2514/6.2020-0557>, AIAA Paper 2020-0557.
- [34] Deparday, J., He, X., Eldredge, J. D., Mullenens, K., and Williams, D. R., "Experimental quantification of unsteady leading-edge flow separation," *Journal of Fluid Mechanics*, Vol. 941, 2022, p. A60. <https://doi.org/10.1017/jfm.2022.319>.
- [35] Gloutak, D., Jansen, K. E., and Farnsworth, J. A., "Aerodynamic Performance of a Finite-Span Wing in a Time-Varying Freestream," *AIAA Journal*, Vol. 62, No. 6, 2024, pp. 2248–2263. <https://doi.org/10.2514/1.J062710>.
- [36] Young, A. M., and Smyth, A. S. M., "Gust–Airfoil Coupling with a Loaded Airfoil," *AIAA Journal*, Vol. 59, No. 3, 2021, pp. 773–785. <https://doi.org/10.2514/1.J059688>.
- [37] Jones, A. R., Cetiner, O., and Smith, M. J., "Physics and Modeling of Large Flow Disturbances: Discrete Gust Encounters for Modern Air Vehicles," *Annual Review of Fluid Mechanics*, Vol. 54, 2022, pp. 469–493. <https://doi.org/10.1146/annurev-fluid-031621-085520>.
- [38] Küssner, H. G., "Zusammenfassender Bericht über den instationären Auftrieb von Flügeln," *Luftfahrtforschung*, Vol. 13, No. 12, 1936, pp. 410–424.
- [39] Wagner, H., "Über die Entstehung des dynamischen Auftriebes von Tragflügeln," *Zamm-zeitschrift Fur Angewandte Mathematik Und Mechanik*, Vol. 5, No. 1, 1925, pp. 17–35.
- [40] Walker, P. B., "Growth of Circulation about a Wing and an Apparatus for Measuring Fluid Motion," Tech. rep., Aeronautical Research Committee, 1931. ARC Report No. 1402.
- [41] Sears, W. R., "Some Aspects of Non-Stationary Airfoil Theory and Its Practical Application," *Journal of the Aeronautical Sciences*, Vol. 8, No. 3, 1941, pp. 104–108. <https://doi.org/10.2514/8.10655>.
- [42] Atassi, H. M., "The Sears problem for a lifting airfoil revisited - new results," *Journal of Fluid Mechanics*, Vol. 141, 1984, p. 109–122. <https://doi.org/10.1017/S0022112084000768>.
- [43] He, X., and Williams, D. R., "Pressure Feedback Control of Aerodynamic Loads on a Delta Wing in Transverse Gusts," *AIAA Journal*, Vol. 61, No. 4, 2023, pp. 1659–1674. <https://doi.org/10.2514/1.J062442>.
- [44] He, X., and Williams, D. R., "Loads and Pressure Characteristics on a Wing in Transverse Traveling-Wave Gusts," *AIAA Journal*, Vol. 63, No. 10, 2025, pp. 4143–4155. <https://doi.org/10.2514/1.J064786>.